
MATERIALS AND COATINGS FABRICATED
BY ADDITIVE TECHNOLOGIES

Experimental Investigation on the EBM-Based Additively Manufactured Prismatic Nickel–Titanium SMA Components

Gozde S. Altug-Peduk^{a,b}, Savas Dilibal^{b,*}, Ola Harrysson^a, and Sunullah Ozbek^c

^a North Carolina State University, Edward P. Fitts Department of Industrial and Systems Engineering, NC, USA

^b Istanbul Gedik University, Mechatronics Engineering Department, Istanbul, Turkey

^c Dogus University, Mechanical Engineering Department, Istanbul, Turkey

*e-mail: savas.dilibal@gedik.edu.tr

Received November 29, 2020; revised January 26, 2021; accepted February 18, 2021

Abstract—Additive manufacturing (AM) of the nickel–titanium (NiTi) shape memory alloys (SMA) have provided novel component solutions with a variety of design configurations in the industry. Electron beam melting (EBM) is a trending metal additive manufacturing process for industrial applications in the field of biomedical and aerospace engineering. In this study, experimental investigations were conducted to reveal the effect of processing conditions on the microstructure and hardness properties of EBM-fabricated nickel–titanium components. Furthermore, detailed microstructural characterizations were performed with a scanning electron microscope, EDS, and XRD for unveiling of the microscopic structure and phase analysis during the layer by layer solidification. The experimental results were systematically evaluated for the powder and the bulk prismatic components, respectively.

Keywords: additive manufacturing, electron beam melting, nickel–titanium shape memory alloy, microstructures

DOI: 10.3103/S1067821221030020

1. INTRODUCTION

Additive manufacturing offers widespread practical applications in the fields of biomedical and aerospace engineering. The implementation of computer-aided disruptive design and manufacturing technologies integrated the design process to the digital manufacturing for creating novel state-of-the-art components. In the digitalized AM process, the components are deposited layer by layer according to the original 3D CAD data in contrast to the traditional subtractive manufacturing techniques [1]. In addition to the digitalized manufacturing, the additive manufacturing of NiTi shape memory alloys (SMAs) accelerated the development of 4D-printing of metallic components for enhanced functionality. The shape recovery of the NiTi SMAs provides the fourth dimension through the adaptation to the surroundings with temperature fluctuation [2].

Many researchers used the laser-based powder bed fusion systems (LPBF) to produce NiTi SMA components [3–5]. However, the Ni-loss by evaporation, the oxygen pick-up, high dislocations density, and the microstructural heterogeneity were mostly observed during the fabrication process. Thus, the electron beam melting (EBM)-based AM process provides alternative solutions for idealized component structure. The EBM system is developed by Arcam AB as a

powder-bed fusion process. Compared to the LPBF, EBM has a greater energy density, higher powder bed temperature, faster scan speed for creating stress-free and impurity relieved parts under a vacuum environment. In addition to these advantages, it provides a higher build rate, higher surface quality on finished parts, and eliminated secondary processing. Design flexibility, and the recyclability of the powders after the building process are recognized as a noticeable functionality for both EBM and LPBF [6]. During the fabrication of fully dense solid parts with EBM, the process parameters optimization without affecting the transformation temperatures with convenient energy input minimizes the impurity pick-up. It develops the functional properties of the final product [7, 8].

Kumar et al. employed laser engineered net shaping technique to study the effect of process parameters on the microstructural and mechanical behavior of the NiTi alloys. The change of laser scan speed, and energy density dictate the observed porosity levels. The highest level of laser density affects the porosity level, precipitates, and martensite phase [9]. Farber et al. stated that martensitic transformation temperatures increase with increasing laser density owing to the evaporation of nickel. Thus further thermal post-processing is applied to control the transformation temperatures for laser based AM systems [10]. Oliveira

Table 1. Optimized process parameters used by Arcam Q10Plus system

Preheating temperature, °C	Layer thickness, μm	Scanning speed, mm/s	Beam current, mA	Focus offset, mA
760	50	1522–4500	2–19	32

et al. referenced that, transformation temperatures and phase structures were varied based on the application location of the laser beam in the as-built sample [11]. They also noted that precipitates were heterogeneously distributed in the microstructure in the as-built sample. Parvizi et al. reviewed the relationship between process parameters and microstructures of additively manufactured NiTi parts [12]. They reported poor surface finish and higher porosity level, which lead to Ni release and weak mechanical properties as a drawback of the used AM process with the production parameter of finer columnar grains in the built direction. Wang et al. studied on the additive manufacturing of NiTi alloy using pre-mixed powders via direct energy deposition (DED), SLM, selective electron beam melting (SEBM). They have also compared the obtained results. They reported that they successfully built solid NiTi samples through the DED and SLM processes even though the formation of unwanted secondary intermetallic phases such as Ti_2Ni , Ni_3Ti . However, they noted that NiTi samples were unable to be fabricated through the SEBM process due to the lack-of fusion between powder particles during the preheating stage [13].

This research aims to fabricate NiTi alloy via EBM and assess the influence of process conditions on the microstructural and hardness properties of the alloy. The present work addresses the details of these issues through a combined effort of powder properties and microstructural analyses. Particularly, in the first stage of this study, powder size, distribution, and morphological behaviors were investigated. In the second stage, the production of the solid samples was performed layer by layer with accelerated e-beam and the melting strategy according to the CAD model of the structure and process parameters, including beam power, scan velocity and operator settings have been optimized. After successfully fabricating the NiTi samples via EBM, the microstructural characterization methods which are scanning electron microscope (SEM) and X-ray diffraction phase analysis (XRD) were applied to solid specimens in order to reveal their phase formations and crystallographic orientations. In the last stage of the study, the hardness properties of EBM-based additively manufactured Ti–55Ni (wt %) samples were examined to evaluate their process-microstructure-property relations.

2. EXPERIMENTAL PROCEDURES

In this study, pre-alloyed nickel-titanium powder (Ti–55 wt % Ni) in the range of 44–149 μm particle

size was used to manufacture Ni–Ti alloy through the EBM-based AM process. The pre-alloyed gas atomized Ni–Ti powders which were provided by ATI Powder, USA were used in the EBM-based AM process. The size distribution of powder was measured with the laser particle size distribution (PSD) method using a Microtrac S3500 particle size analyzer. Tapped density measurement was applied with a Quantachrome Autotap Analyzer according to the ASTM B527-14 standard, and the flow rate was measured with hall a flowmeter funnel in compliance with the ASTM B703-10 standard. Powder characterization and related analysis were conducted using optical microscopy, SEM, and EDS. For the microscopic investigation, a decent amount of powder particles were hot mounted, ground, polished following to the metallographic sample preparation steps. After polishing process, the samples were etched 20 seconds with the Kroll's reagent which contains 2% HF, 5% HNO_3 , 93% distilled water for the cross-sectional microstructural analysis. The morphological features of the NiTi powders and as-built specimens were initially defined with the Hirox KH7700 digital optical microscope. SEM observations were performed on a Jeol 6010LA scanning electron microscope with fully integrated EDS for detailed microscopic analysis. The XRD analysis of the samples was performed to determine the crystal structures and phase identification of the samples. The XRD scans were conducted using a Rigaku Smart Lab Diffractometer at 25°C with $\text{CuK}\alpha$ radiation ($\lambda = 0.154 \text{ nm}$), a nickel filter and silicon powder as standard reference material. The XRF analysis was made using Niton XL2 XRF machine with a 2W X-ray tube and a spot size of 8 mm collimation. The error limit of the analyzer is 0.1%.

The NiTi solid samples were fabricated using an Arcam Q10 Plus EBM machine system in a vacuum atmosphere for 6 h. In the manufacturing process, the optimization of process parameters is the most significant factor for the EBM method as well as for other layered production methods. The design methodology was developed considering the previous research in the literature and Arcam's optimized process theme for the Ti–6Al–4V alloy [14]. The process parameters used in the EBM fabrication process were listed in Table 1. In the initial stage of the process, the powder bed is preheated to 760°C in order to improve the conductivity and interconnection of the powders and to prevent their repulsion inside the chamber [15]. The layer thicknesses of 50 μm were used during the building process. The scanning speed, beam current, and maximum current parameters were optimized to pro-

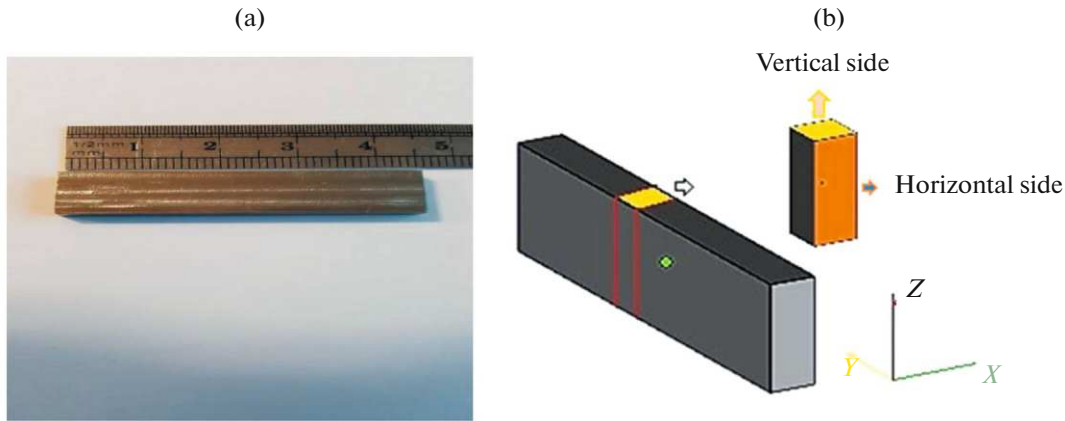


Fig. 1. (a) Electrical discharge machined EBM-based additively manufactured NiTi component. (b) Sectioned microstructure of the prismatic NiTi component.

duce fully dense NiTi alloy at a 850°C target operating temperature. One of the as-built NiTi samples with the dimensions of $50 \times 5 \times 16$ mm is shown in Fig. 1a. No additional secondary heat treatment was applied to the electron beam powder bed fusion fabricated NiTi SMA components.

For microstructural characterization, the electron beam powder bed fusion fabricated samples were sectioned vertical and horizontal to the build direction (z) as schematically illustrated in Fig. 1a. Each section was hot mounted, ground, polished, and etched with an etchant (% 3.2 HF, % 14.6 HNO₃, distilled water) for 40 s. The Vickers micro-hardness test was performed with a Shimadzu G21 series micro-indentation hardness tester on polished samples at room temperature under a 100 g load (HV0.1). Eleven measurements were taken at points distanced 1 mm apart across the straight line of the specimen, starting from the bottom layer to the top surface. A detailed hardness profile was created with the measured hardness values.

3. RESULTS

3.1. Physical and Microstructural Properties of the Powder

The average powder density value was calculated to 4.1485 g/cm³, and the flowability index was obtained as 20.712 (s/50 g). Based on the number distribution the median particle size distribution (PSD) of Ti–55 wt % Ni powders was obtained as 65.88 μm, as shown in Fig. 2a. As a result of the SEM examination, spherically shaped particles were observed, as shown in Fig. 2b. Satellite finer powder particles which attach to the surface of the coarser particles and conducted with gas atomization process, typical trapped porosity were revealed in low concentrations (Fig. 2c). In order to confirm the existing amount of the Ni and Ti concentrations in pre-alloyed powder particles, powder

samples were subjected to an energy-dispersive X-ray spectroscopy (EDS) analysis. According to the EDS analysis results, EDS element mapping images exhibit the homogeneous distribution of each Ni and Ti element for the Ni–Ti alloy formation (Fig. 2b). Figure 2d represent the XRD analysis results with diffraction patterns in the 2Theta range of 25°–80°. Moreover, in terms of peak analysis, martensite (M) in monoclinic form and austenite (A) in the cubic structure was observed. Additionally, the Ti₂Ni intermetallic phase and free Ni were also observed in the EDS mapping results.

The cross-sectional microstructure of the Ni–Ti powder showed an equiaxed dendritic structure as a consequence of the formation and growth of new dendrites in random orientations within a solid-liquid zone called as “mushy zone” as shown with arrows in Fig. 2c. As a part of the dendritic solidification process, darker contrast was observed near the roots of dendrites due to the solute enrichment. As shown in the circle in the same figure, the black voids were entrapped by the growing dendrites.

In the EBM process, after loading the powder, which is used as a bulk material to the hoppers, the rake test is performed to adjust the raking speed and to obtain a homogeneous powder layer on the powder bed, as seen in Fig. 3. In this stage, particularly powder flowability plays a key role together with PSD since an optimized amount of powder spreads to the build table, and higher-layer densities are provided according to the flow rate of the powders. During the further stages, sufficient beam energy cannot reach the substrate material and cause the incomplete fusion, lower deposition rate for the new powder layer, void spaces in the layers, and low mechanical properties in the build direction due to the lower layer densities [16]. For the flow rate of the powders, surface morphology and cohesion are other essential factors. It is evident that the powder flowability increases with fine powders and decreases with the presence of coarse and

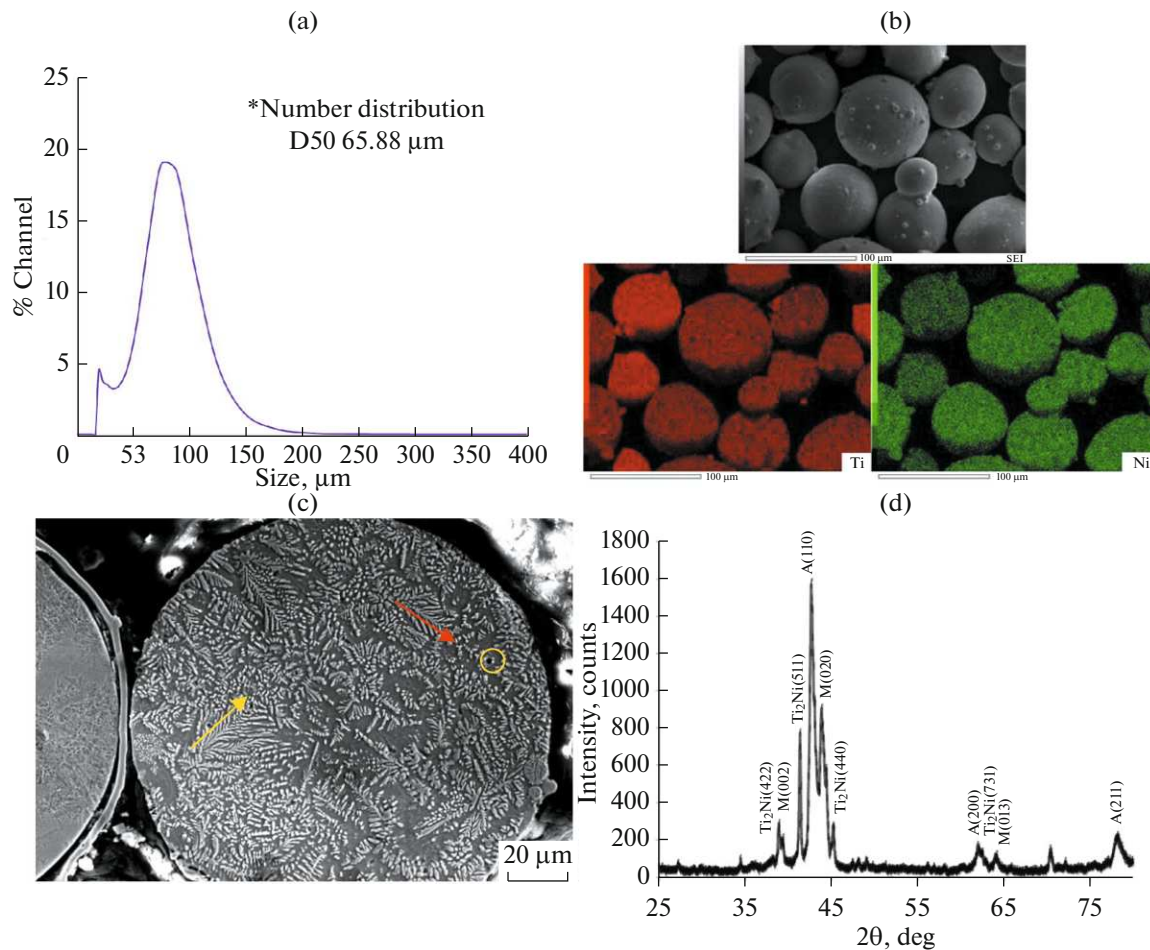


Fig. 2. (a) Powder size distribution plot, (b) EDS element mapping images for Ti and Ni, (c) SEM micrograph showing the cross-section, (d) XRD pattern of the Ti–55 wt % Ni powder.

irregular particles. When the particle surface is investigated, it is found that splat caps and satellites lead mechanic interlocking between the particles as increasing the interparticle forces, and resulting in lower flowability as shown in Fig. 3. In the literature, simulations were conducted to mimic the particle behavior and flowability characteristics under the gas pressure environment and concluded that, for the coarse particles, the total force is calculated as gravitational force and the sum of interparticle contact forces (F_n , and F_c), and cohesion force (F_{ijk}) based on the Hertz–Mindlin theory (Eq. (1)) [17].

$$\sum F = mg + F_n + F_c + F_{ijk}. \quad (1)$$

Chen et al. [18] performed numerical simulations using the discrete element method to investigate the powder spreading process. They revealed that the effect of friction forces on particles from the substrate increased with the increasing spreading speed under the strong pressure of the roller, and powders started to lose coordination and decreased a gap without laying on the substrate. Considering the literature reviews

and simulation results, the scanning parameters were adjusted to overcome the challenge of coarse and irregular powders with satellite particles spreading on the substrate and having high density fully melted layers in the current study.

3.3. Microstructural Characterization of As-built Specimens

The result of the XRF analysis for an as-built sample is displayed in Fig. 4, where the compositional data expressed in weight percent for the major elements (54.9% Ni and 44.9% Ti).

In the etched condition, Fig. 5a demonstrates that the matrix phase of the alloy is formed as *B2* austenite phase. In the micrograph of Fig. 5b, it was observed that the austenitic Ni–Ti matrix consisted of 200 μm wide grains, and the grains were surrounded by a network structure, as shown in Fig. 5b.

In the direction of solidification on the cross-section sample, first, the section from the top layer to the center and then from the center to the first layer was

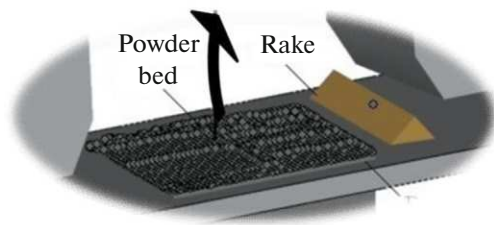
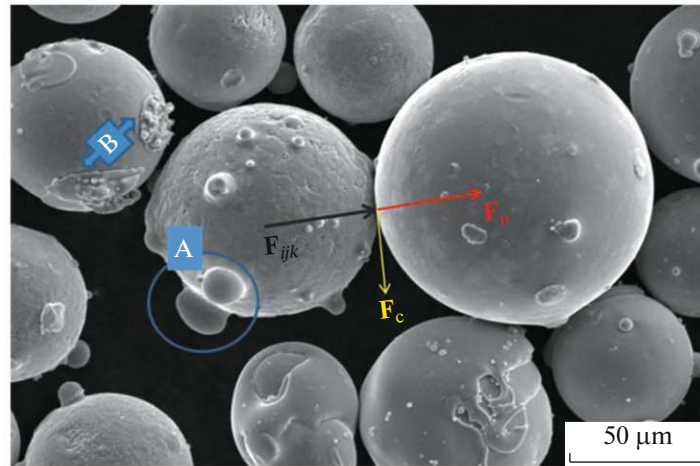


Fig. 3. SEM micrograph of the NiTi powder, showing the powder interlocking, satellite formation (A), and splat caps on the powder surface (B).

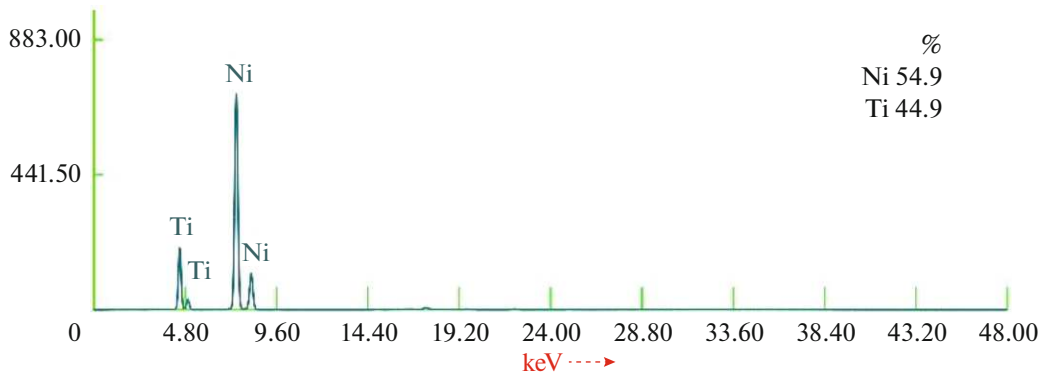


Fig. 4. A typical XRF spectrum of NiTi as-build sample.

examined in two different areas. As seen in Fig. 6a, homogeneous solidification and columnar grain structure were observed along the build direction. Full solidification was achieved during the melting of the layers. In Fig. 6b, needle-like structures were found at the intersection of the boundary of the grain at high magnification (indicated in a circle). In order to determine the precipitate and phase compositions, semi-quantitative regional/spot EDS analysis was performed at spot size 70 on this image in the regions marked in Fig. 7. Point reference 1 was located in the matrix region, while point reference 2 was located in the precipitate area. The results of this analysis are

exhibited in the corresponding EDS spectrums, respectively (Fig. 8). Both of the EDS spectrums substantiated that EBM-fabricated NiTi specimens constituted Ni and Ti in different amounts. Spot 1 shows a near-equiatomic NiTi composition, following as 49.86 at % Ni, and 50.14 at % Ti. In spot 2, major Ni and Ti were detected in the atomic percentage of 54.48 and 45.52, respectively. XRD analysis was performed to confirm the EDS results and to evaluate the transformations occurring during layer by layer NiTi alloy fabrication process. The diffractogram presented in Fig. 9 consists of *B2*-austenite and *B19'*-martensite X-ray lines as dominant diffraction patterns, which is

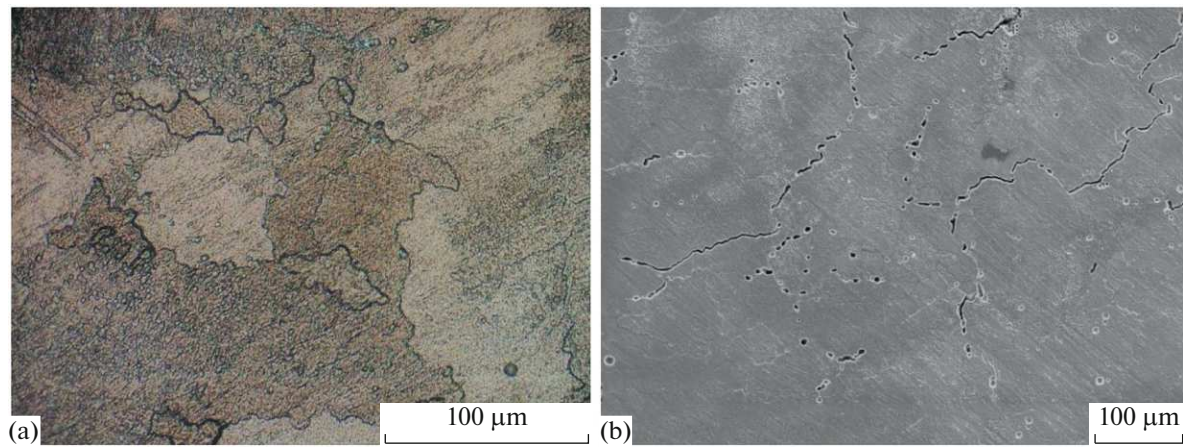


Fig. 5. (a) Optical micrograph. (b) Secondary electron SEM images of vertical side specimen in etched condition.

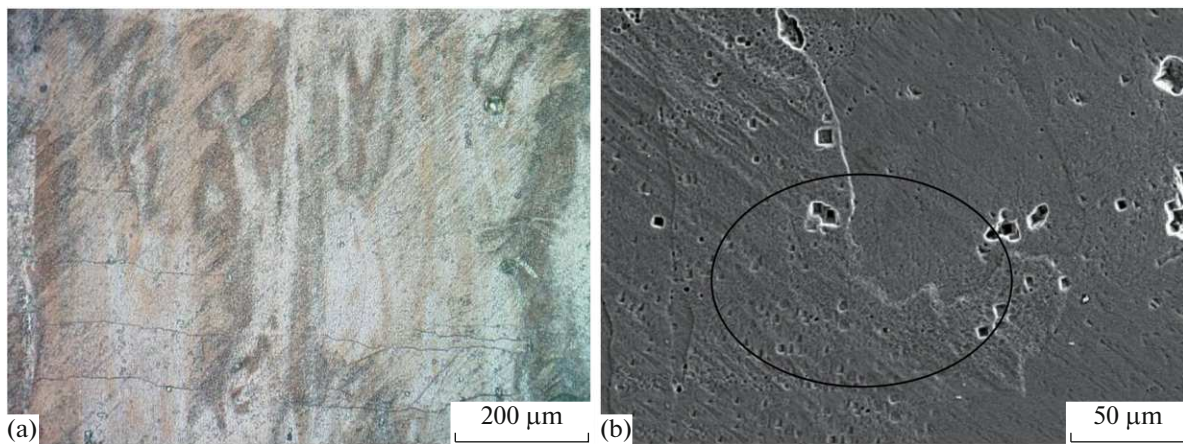


Fig. 6. (a) Optical micrograph, (b) secondary electron SEM images of horizontal side specimen in etched condition.

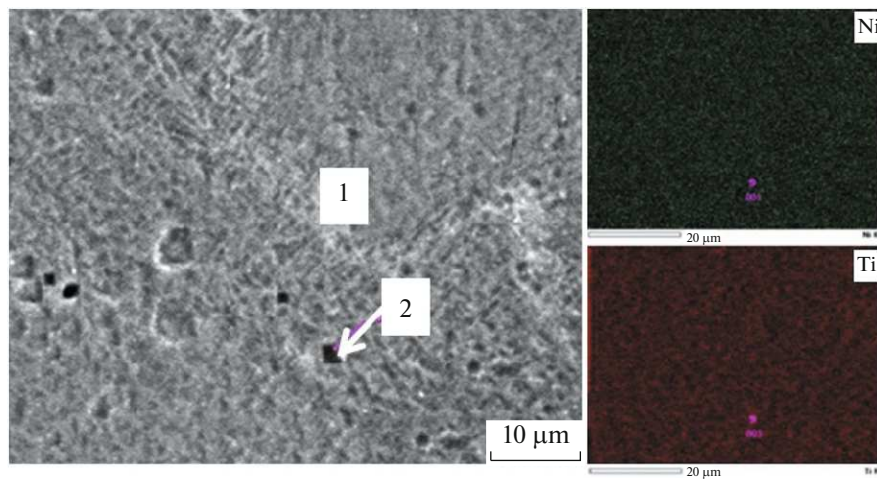


Fig. 7. Secondary electron SEM image and EDS mapping for Ni and Ti.

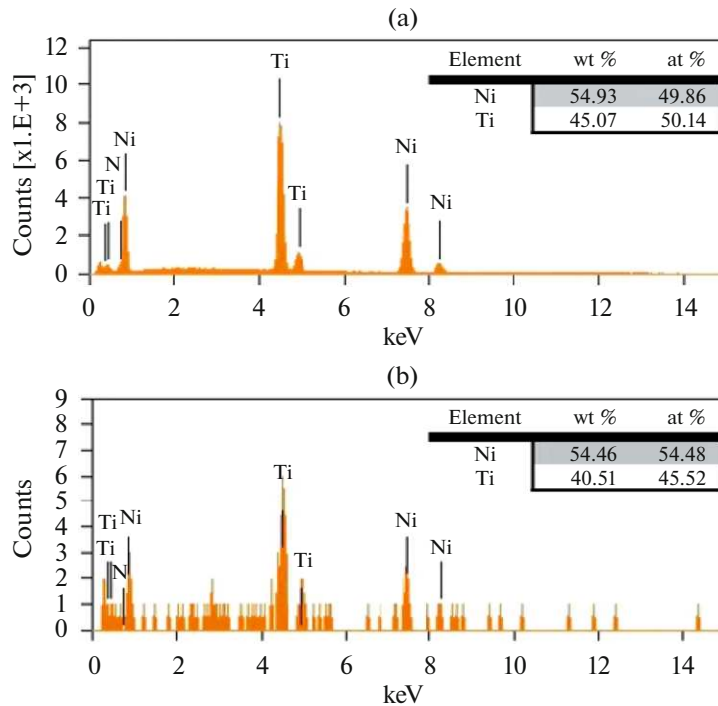


Fig. 8. Corresponding EDS spectra of the matrix (a) and precipitated area (b) of the NiTi component.

typical for a two-phase (B2-austenite and B19'-martensite) near-equiatomic Ti–Ni SMA.

3.4. Micro-Hardness Behavior

Vickers microhardness measurements were performed on the EBM-fabricated specimen to make a precise evaluation and examine the state of occurrence of microstructural formations on the hardness values between the layers. Three main points were measured at the sample edges with $HV = 271 \pm 10$ and eight points distributed along the main part of the sample with $HV = 382 \pm 16$ from bottom to the top layer. Microhardness measurement close to spot 2 (Fig. 7) revealed about $417 HV_{0.1}$ as the maximum hardness value.

4. DISCUSSION

Powder density, size distribution, flowability, and morphological features of the powders are important characteristics that influence electron beam deposition on the substrate during the building process. Dependent on the powder manufacturing methods, powder quality is highly affected by the surface formation, microstructure, and porosity amount. Particle sizes were determined within the desired range and in accordance with the particle size distribution results [19]. Therefore, pre-alloyed NiTi powder produced by gas atomization process provided very desirable properties to fulfill the EBM fabrication process require-

ments. However, the existence of the trapped gas pores, and satellites particles affect the density of the EBM-fabricated parts. Optimization of the process parameters, especially the increase of the preheating temperature, varying the scanning speed, and beam current allowed us to control the powder stock and melt-pool formation. Thus most of the entrapped gas pores were eliminated, and fully dense EBM parts were fabricated.

Microstructural characteristics of NiTi alloys are generally associated with titanium reactivity in the structure and melting process during the manufacturing process of the alloy. The alloys produced with conventional methods are highly subjected to contaminations, due to the carbon reactivity from the graphite crucible. The arc melting alloys constitute secondary Ni_xTi_y phases with lower homogeneity than the induction melted alloys. Due to the extreme interest in the oxygen of these intermetallic phases, the oxides form in the range of 400–800 ppm with Ti elements. These particles and porosities in the microstructure can be critical for the occurrence of the martensitic transformation. In the matrix of wire-shaped NiTi alloys, these inclusions and oxide particles are noticed as needle-like structures with homogeneous distribution in white contrast around $6 \mu\text{m}$ in lengths [20]. In the Ni–Ti phase diagram, which was developed by Masalski et al. [21] and revised by Otsuka et al. [22], in the equilibrium conditions there are three major intermetallic phases following as; $TiNi_3$, $TiNi$ and, Ti_2Ni phases. The $TiNi$ region is surrounded by Ti_2Ni (face-

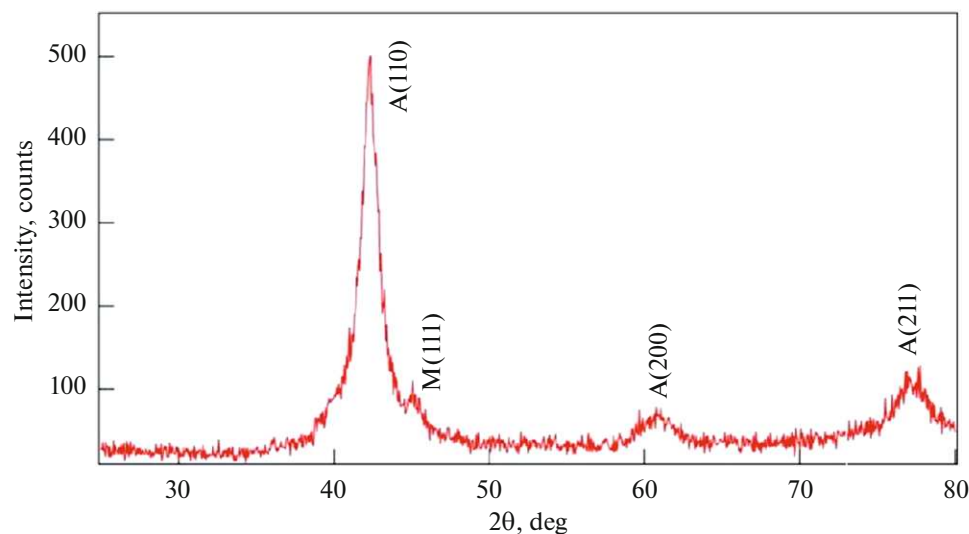


Fig. 9. XRD spectra for the as-built NiTi component.

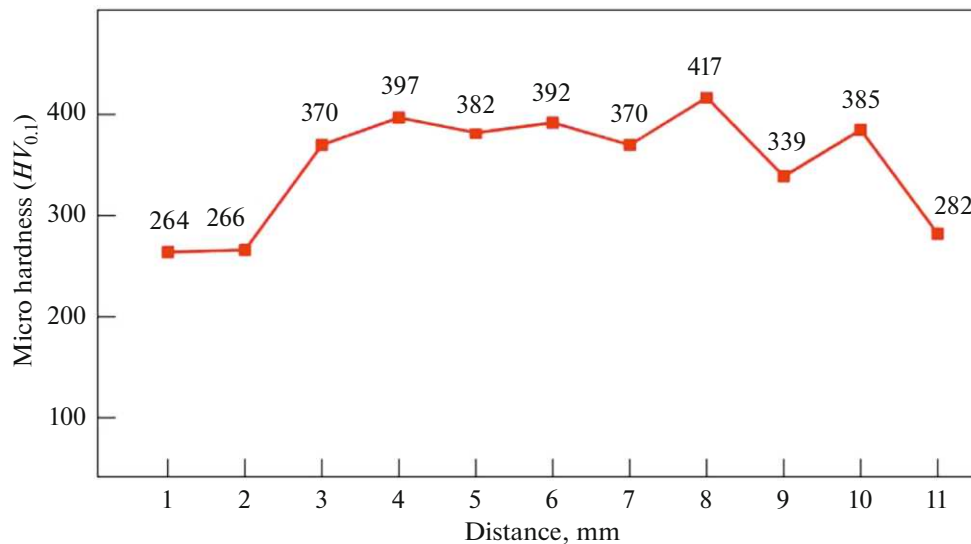


Fig. 10. Hardness profile for as-fabricated NiTi component.

centered cubic, fcc with 96 atoms per unit cell) on the left side and TiNi_3 (hexagonal close-packed, hcp) on the right side. Khamei et al. proposed Ni_3Ti precipitate forms during the cooling stage from casting and/or hot working on the grain boundaries and within the matrix as a needle-like structure and a Widmanstatten pattern. Dynamically recrystallized grains nucleate on the grain boundaries by the bulging mechanism and create the necklace structure as seen in Figs. 5a, 5b. On the other hand, the presence of precipitates evolves the nucleation of pores and assisted in pore formation at the grain boundaries [23]. Since pore formation and pore growth are a diffusion-controlled process, increasing solidification time also

increases the pore area [24]. Thier et al. showed that fine shrinkage pores were observed as a white-shaded area around the polygonal Ti_2Ni particles as a result of the solidification process, which occurs due to the high cooling rates with losses in Ti content within the matrix to a stabilization of the austenitic structure [25]. NiTi samples fabricated via powder metallurgy, Ti_2Ni , TiNi , TiNi_3 , and residual Ni and Ti structures were indicated. With increasing sintering temperature, residual Ti disappeared, and dark black pore regions appeared. Increasing sintering time caused the formation of coherent Ti_3Ni_4 precipitates as needle-like structures during the slow cooling of the samples. The TiNi_3 phase, which formed a network within the NiTi

matrix, was noticed in the form of small particles [26]. Despite the parts manufactured via casting, and conventional PM, which contain Ni and Ti-based intermetallic phases, TiNi₃ precipitates were not observed in the microstructures of the specimens produced via SLM [4]. Powder-based metal AM techniques produce anisotropic microstructures with elongated grains in the build direction and the crystallization depends on the process parameters related to the layer thickness of the powders, scanning velocity, and beam power [27]. During the EBM process, inside the building chamber, each molten metal layer is formed under the heat effect as a result of the epitaxial growth and nucleation of particles in the microstructure. In the cooling stage of the metal, the temperature decrease under the transition temperature, based on the nucleation mechanism, phase transformations take place and new transformation phases occur [28]. Particularly it is also known that the existence of the secondary particles promotes the nucleation of martensite plates. The XRD results for the as-fabricated sample indicated the two-phase diffraction patterns. Thus, the results are in accordance with the theoretical predictions and previous investigations. The group of lines in the 38 to 46 deg. angular range represents a superposition of (110) of A at 42.3° and (110) of M at 38.2°, (002) of M at 39.1°, (11 $\bar{1}$) of M at 41.1°, (020) of M at 44.0° and (111) of M at 45.1° [29, 30]. Since preheating at 760°C creates ageing affect for the NiTi alloy, and correlates with the secondary phase in the microstructure, Ti₃Ni₄ and TiNi₃ phases should be formed with decreasing Ni content in the B2-austenite matrix. If the actual parameters are considered as of its rhombohedral lattice ($a = 6.61$ nm and alpha angle of 113.6 deg.), the position of the Ti₃Ni₄ line must be at 107.8 deg. Although this interpretation is in correlation with EDS and SEM observations from Fig. 7 (corresponding to spot 2 analysis), no strong signal was detected in the XRD results regarding these intermetallic phases between 25°–80° 2 θ degrees. Thus, no signs of the presence of Ti₃Ni₄ and TiNi₃ phases have been revealed, and this is inherent in equiatomic TiNi SMA. Further TEM examination will be conducted to reveal the exact presence of the intermetallic phases with their locations.

The measured Vicker's hardness profile was evaluated for comparison with literature values. Early studies reported that increasing Ni composition exhibited increasing hardness values for NiTi alloys, and maximum hardness values were obtained from the alloy Ti–55Ni in the quenched condition due to precipitation hardening by secondary phases. Application of solution hardening on the B2 austenite condition and immediately water quenching provide the formation of nano- and micro-precipitates. These precipitates carry out narrow channels to create hardening similar to the Orowan mechanism. Additionally, coherent precipitates contribute to the hardening mechanism as

it is generating substantial strain in the matrix. Adharapurapu et al. observed TiNi₃ blocky precipitates along the grain boundary as a stable equilibrium phase and Ti₃Ni₄ and Ti₂Ni₃ metastable phases. Samples aged at 500°C exhibited high hardness values due to the presence of coherent Ti₃Ni₄ precipitates within the matrix, and with increasing, aging temperatures to 1000°C, the formation of TiNi₃ precipitates improved the strength and ductility with a good balance [31]. Lucas et al. reported a 225 HV for Ti–55Ni alloy produced via the vacuum melt casting method. An increase in hardness value (280 HV) was achieved along with the formation of the R phase and Ti₃Ni₄ precipitates after the heat treatment application [32]. Ti–55Ni alloy produced by SLM has reached 540–735 HV hardness values as a result of secondary aging applications [33]. The homogeneous distribution of Ti₃Ni₄ precipitates within the NiTi matrix at low aging temperatures enhance the hardness, yield strength, and fatigue resistance of the NiTi SMAs associated with critical stress for slip deformation and an impediment to dislocation motion [34]. It is worth noting that grain boundaries, secondary phase particles, dislocations, and porosity levels influence the hardness and mechanical properties of the alloys. In AM techniques, process variables, grain refinement [35] due to rapid cooling by blocking dislocation motion, initiation of the formation of martensitic grains, and prevention of crack formation depending on the selected parameters are the main factors that increase the microhardness in the final part. In this study, compared to casting and SLM methods, higher hardness values were obtained for EBM NiTi sample in as-fabricated condition without any post-processing heat treatment application because of the ageing affect during the preheating and the presence of a martensitic TiNi phase formation, which contributes to the increase in hardness value, and superelastic behavior. The cyclic loading experiments reveal the potential application capabilities of the manufactured product [36, 37].

5. CONCLUSIONS

In this study, microstructural characteristics of powder and bulk Ti 55% Ni alloy, which was fabricated via the EBM additive manufacturing method, were investigated. In the microscopic examinations, the particle sizes were determined within the desired range. It was verified that these values were in accordance with the SEM investigations. Although the presence of the splat cap formation, and satellite particles as a result of the gas atomization process, high packaging density and high deposition rate were obtained during the building process. As a result of EDS and XRD analysis, the NiTi alloy composition was confirmed to be near-equiatomic NiTi, which consists of austenite parent phase, martensite, and

Ti₂Ni intermetallic phase. The detected phases and their crystallographic orientations were found to be in agreement with the literature. The examined properties, size, distribution, density, flow rate, composition, and microstructures of the NiTi powder are conducted to be appropriate for the EBM-based AM process. Microstructural properties of the solid samples produced by the EBM method are influenced by all processing steps, including preheating, melting, and cooling. In the development production, especially the scanning speed and beam current values were adjusted as well as a number of repetitions for the preheating stage. As soon as achieving the successful results, developed process parameters were applied to the final production for the bar samples. As a result of XRD analysis, the austenite phase in the cubic structure was observed as the dominant phase in the structure and the martensite phase in monoclinic form, were revealed. After the microhardness measurement, hardness values were obtained between 264 and 417 HV. Therefore, additive manufacturing provides an attractive processing method for Ni-Ti alloys to overcome manufacturing challenges with layer by layer fabrication principles and design flexibilities. The shape memory and superelastic responses of the additively manufactured EBM Ni-Ti alloy will be investigated in the future work.

CONFLICT OF INTEREST

The authors state that they have no conflict of interest.

REFERENCES

1. ASTM Committee F42 on Additive Manufacturing Technologies.
2. Lee, A.Y., An, J., and Chua, C.K., Two-way 4D printing: A review on the reversibility of 3D-printed shape memory materials, *Engineering*, 2017, vol. 3, no. 5, p. 663.
3. Shishkovsky, I., Yadroitsev, I., and Smurov, I., Direct selective laser melting of nitinol powder, *Phys. Procedia*, 2012, vol. 39, p. 447.
4. Jahadakbar, A., Moghaddam, N.S., Amerinatanzi, A., Dean, D., and Elahinia, M., Mechanical evaluation of the SLM fabricated, stiffness-matched, mandibular bone fixation plates, *Proc. SPIE*, 2018, vol. 10596, p. 1059610.
5. Shiva, S., Palani, I.A., Mishra, S.K., Paul, C.P., and Kukreja, L.M., Investigations on the influence of composition in the development of Ni-Ti shape memory alloy using laser based additive manufacturing, *Opt. Laser Technol.*, 2015, vol. 69, p. 44.
6. Altug-Peduk, G.S., Dilibal, S., Harrysson, O.L.A., Ozbek, S., and West, H., Characterization of Ni-Ti alloy powders for use in additive manufacturing, *Russ. J. Non-Ferrous Met.*, 2018, vol. 59, p. 433.
7. Murr, L.E., Metallurgy of additive manufacturing: Examples from electron beam melting, *Addit. Manuf.*, 2015, vol. 5, p. 40.
8. Frigola, P., Harrysson, O.L.A., and Ramirez, D.A., Fabricating copper components with electron beam melting, *Adv. Mater. Processes*, 2014, vol. 152, p. 20.
9. Kumar, S., Marandi, L., Balla, V.K., Bysakh, S., Piorenek, D., Eggeler, G., Das, M., and Sen, I., Microstructure—Property correlations for additively manufactured NiTi based shape memory alloys, *Materialia*, 2019, vol. 8, p. 15.
10. Farber, E., Zhu, J., Popovich, A., and Popovich, V., A review of NiTi shape memory alloy as a smart material produced by additive manufacturing, *Mater. Today: Proc.*, 2020, vol. 30, p. 761.
<https://doi.org/10.1016/j.matpr.2020.01.563>
11. Oliveira, J.P., Cavaleiro, A.J., Schell, N., Stark, Andreas, Miranda, R.M., Ocana, J.L., and Braz Fernandes, F.M., Effects of laser processing on the transformation characteristics of NiTi: A contribute to additive manufacturing, *Scr. Mater.*, 2018, vol. 152, p. 124.
12. Parvizi, S., Hashemi, S.M., Asgarinia, F., Nematollahi, M., and Elahinia, M., Effective parameters on the final properties of NiTi-based alloys manufactured by powder metallurgy methods: A review, *Prog. Mater. Sci.*, 2020, vol. 117, p. 100739.
<https://doi.org/10.1016/j.pmatsci.2020.100739>
13. Wang, C., Tan, X.P., Du, Z., Chandra, S., Sun, Z., Lim, C.W.J., Tor, S.B., Lim, C.S., and Wong, C.H., Additive manufacturing of NiTi shape memory alloys using pre-mixed powders, *J. Mater. Process. Technol.*, 2019, vol. 271, p. 153.
14. Yoder, S., Morgan, S., Kinzy, C., Barnes, E., Kirka, M., Paquit, V., Nandwana, P., Plotkowski, A., Dehoff, R.R., and Babu, S.S., Characterization of topology optimized Ti-6Al-4V components using electron beam powder bed fusion, *Addit. Manuf.*, 2018, vol. 19, pp. 184–196.
15. Ataee, A., Li, Y., and Wen, C., Metal scaffolds processed by electron beam melting for biomedical applications, in *Metallic Foam Bone, Processing, Modification and Characterization and Properties*, Elsevier Science, 2017, p. 83.
16. Vock, S., Klöden, B., Kirchner, A., et al., Powders for powder bed fusion: a review, *Prog. Addit. Manuf.*, 2019, vol. 4, p. 383.
17. Espiritu, E.R.L., Kumar, A., Nommeots-Nomm, A., et al., Investigation of the rotating drum technique to characterise powder flow in controlled and low pressure environments, *Powder Technol.*, 2020, vol. 366, p. 925.
18. Chen, H., Chen, Y., Liu, Y., Wei, Q., Shi, Y., and Yan, W., Packing quality of powder layer during counter-rolling-type powder spreading process in additive manufacturing, *Int. J. Mach. Tools Manuf.*, 2020, vol. 153, article no. 103553.
19. Ashgriz, N., *Handbook of Atomization and Sprays: Theory and Applications*, Springer, 2011.
20. Shabalovskaya, S., Anderegg, J., and Van Humbeeck, J., Recent observations of particulates in Nitinol, *Mater. Sci. Eng., A*, 2008, vol. 481, p. 431.
21. Massalski, T.B., Okamoto, H., and Subramanian, P.R., *Binary Alloy Phase Diagrams*, Materials Park, OH: ASM Int., 1990, vol. 3, p. 2874.
22. Otsuka, K. and Wayman, C.M., *Shape Memory Materials*, Cambridge: Cambridge Univ. Press, 1988, p. 49.

23. Khamei, A. and Dehghani, K., Microstructural evolution during the hot deformation of Ti-55Ni (at. pct) intermetallic alloy, *Metall. Mater. Trans. A*, 2010, vol. 41, p. 2595.
24. Roy, N., Samuel, A.M., and Samuel, F.H., Porosity formation in Al-9 wt % Si-3 wt % Cu alloy systems: Metallographic observations, *Metall. Mater. Trans. A*, 1996, vol. 27, p. 415.
25. Thier, M., Hühner, M., Kobus, E., Drescher, D., and Bourauel, C., Microstructure of As-cast NiTi alloy, *Mater. Charact.*, 1991, vol. 27, p. 133.
26. Mohd Zaki, H.H., Solid state synthesis of NiTi, *MSc Thesis*, Univ. of Western Australia, 2011.
27. Bormann, T., Muller, B., Schinhammer, M., Kessler, A., Thalmann, P., and Wild, M., Microstructure of selective laser melted nickel-titanium, *Mater. Charact.*, 2014, vol. 94, p. 189.
28. Sames, W.J., List, F.A., Pannala, S., Dehoff, R.R., and Babu, S.S., The metallurgy and processing science of metal additive manufacturing, *Int. Mater. Rev.*, 2016, vol. 61, no. 5, p. 315.
29. Prokoshkin, S.D., Korotitskiy, A.V., Brailovski, V., Turenne, S., Khmelevskaya, I.Yu., and Trubitsyna, I.B., On the lattice parameters of phases in binary Ti-Ni shape memory alloys, *Acta Mater.*, 2004, vol. 52, no. 15, pp. 4479-4492.
30. Prokoshkin, S.D., Korotitskiy, A.V., Brailovski, V., Inaekyan, K.E., and Dubinskiy, S.M., Crystal lattice of martensite and the reserve of recoverable strain of thermally and thermomechanically treated Ti-Ni shape memory alloys, *Phys. Met. Metallogr.*, 2011, vol. 112, no. 2, pp. 170-187.
31. Adharapurapu, R.R., Jiang, F., and Vecchio, K.S., Aging effects on hardness and dynamic compressive behavior of Ti-55Ni (at %) alloy, *Mater. Sci. Eng., A*, 2010, vol. 527, p. 1665.
32. Lucas, F.L.C., Guido, V., Kafer, K.A., Bernardi, H.H., and Otubo, J., ECAE processed NiTi shape memory alloy, *Mater. Res.*, 2014, vol. 17, p. 186.
33. Saedi, S., Turabi, A.S., Andani, M.T., Moghaddam, N.S., Elahinia, M., and Karaca, H.E., Texture, aging, and superelasticity of selective laser melting fabricated Ni-rich NiTi alloys, *Mater. Sci. Eng., A*, 2017, vol. 686, p. 8.
34. Jiang, S.Y., Zhao, Y.N., Zhang, Y.G., Hu, L., and Liang, Y.L., Effect of solution treatment and aging on microstructural evolution and mechanical behavior of NiTi shape memory alloy, *Trans. Nonferrous Met. Soc. China*, 2013, vol. 23, p. 3658.
35. Zuback, J.S. and DebRoy, T., The hardness of additively manufactured alloys, *Materials* (Basel), 2018, vol. 11, p. 28.
36. Dilibal, S., Hamilton, R.F., and Lanba, A., The effect of employed loading mode on the mechanical cyclic stabilization of NiTi shape memory alloys, *Intermetallics*, 2017, vol. 89, p. 6.
37. Moghaddam, N.S., Saedi, S., Amerinatanzi, A., Hinojos, A., Ramazani, A., Kundin, J., Mills, M.J., Karaca, H., and Elahinia, M., Achieving superelasticity in additively manufactured NiTi in compression without post-process heat treatment, *Sci. Rep.*, 2019, vol. 9, p. 7.